Acta Materialia 140 (2017) 87–96

Contents lists available at ScienceDirect

Acta Materialia

journal homepage: www.elsevier.com/locate/actamat

Full length article

General evolution equation for the specific interface area of dendrites during alloy solidification

H. Neumann-Heyme [a], K. Eckert [a, b], C. Beckermann [c, *]

[a] Helmholtz-Zentrum Dresden-Rossendorf (HZDR), 01314, Dresden, Germany
[b] Institute of Process Engineering, Technische Universität Dresden, 01062, Dresden, Germany
[c] Department of Mechanical and Industrial Engineering of Iowa, University of Iowa, Iowa City, IA, 52242, USA

ARTICLE INFO

Article history:
Received 10 July 2017
Accepted 9 August 2017
Available online 11 August 2017

Keywords:
Dendritic solidification
Interfacial area
Phase-field simulation
Synchrotron X-ray tomography experiments

ABSTRACT

The specific area of the solid-liquid interface of an assembly of dendrites is an important integral measure of the morphology of the microstructure forming during alloy solidification. It represents the inverse of a characteristic length scale and is needed for the prediction of solidification defects and material properties. In the present study, the evolution of the interfacial area of dendrites is analysed using 3D phase-field simulations. A general evolution equation is developed for the specific interface area as a function of time and solid volume fraction that accounts for the effects of growth, curvature-driven coarsening and interface coalescence. The relation is validated using data from previously performed synchrotron X-ray tomography and isothermal coarsening experiments. It is found to be valid for arbitrary and even varying cooling rates and for a wide range of binary alloys. The rate constant in the evolution equation is successfully related to alloy properties.

1. Introduction

Dendrites are the primary microstructure in virtually all metal alloys solidified from the melt. Their morphology is critical to the formation of solidification defects, such as porosity, cracks and macrosegregation. Dendrites also control the distribution of alloying elements on a microscopic scale and thereby the amount and spatial arrangement of secondary phases, which in turn strongly affect the properties of solidified materials. Understanding the evolution of dendrites during alloy solidification is thus of both fundamental and technological interest [1]. The most common measure for characterizing solidification microstructures and correlating material properties is the secondary dendrite arm spacing. Clearly, this spacing is an incomplete description of the complex shape of dendrites. As described in our earlier work on this topic [2], the specific area of the solid-liquid interface is an integral measure that characterizes the overall morphology in a more general sense [3,4]. The specific interface area S_s is defined as the area of the solid-liquid interface A per volume of the enclosed solid phase V_s,

$$S_s = A/V_s \tag{1}$$

The inverse of the specific interface area can be considered a characteristic length scale of the microstructure. A similar integral measure is the interfacial area density or concentration S_V. It is defined as the interface area A divided by the sample volume V containing both solid and liquid phases,

$$S_V = A/V = g_s S_s \tag{2}$$

where $g_s = V_s/V$ is the solid volume fraction. The interfacial area density is a key ingredient in volume-averaged (macroscopic) models of alloy solidification [5]. It is needed, for example, in the modeling of microsegregation and of melt flow through the semi-solid mush, the permeability of which is directly related to S_V via the Kozeny-Carman relation $P \sim (1-g_s)^3/S_V^2$ [6].

Under isothermal conditions, the interface area decreases continually due to surface energy driven coarsening, even though the amount of solid does not change. This temporal variation can be described by a classical coarsening law of the form [3]

$$S_s^{-1} = \left(S_{s0}^{-n} + Kt\right)^{1/n} \tag{3}$$

where S_{s0}, n, K, and t are specific interface area at $t = 0$, inverse

* Corresponding author.
E-mail address: becker@engineering.uiowa.edu (C. Beckermann).

http://dx.doi.org/10.1016/j.actamat.2017.08.021
1359-6454/

coarsening exponent, coarsening rate constant, and time, respectively. An exponent of $n = 3$ has been firmly established for volume diffusion-limited coarsening by both experiments and theory. It was first obtained in the LSW theory for Ostwald ripening [7–9] that describes the evolution of a system of dispersed spherical particles in the long-time limit. Although the LSW theory assumes spherical particles and $g_s \to 0$, $n = 3$ has been found to be valid for more general geometries [3,10], including morphologies that are initially dendritic, and for higher solid volume fractions, e.g. Ref. [11]. The coarsening rate constant K is generally a function of the solid fraction. More recently, a LSW-type model has been derived for the important case of concurrent growth and coarsening [12]. Although this model is also limited to low g_s, $n = 3$ was obtained even in the presence of net solidification.

As opposed to pure coarsening, solidification implies that the system is not isothermal (i.e., the cooling rate $\dot{T}$ is non-zero) and the solid fraction g_s increases with time. Initially, the growth of the solid leads to an increase in the interface area. However, at higher solid fractions the evolution of the solid morphology becomes strongly affected by solutal interactions and by interface coalescence, which causes the interface area to decrease. For pure growth processes, in the absence of coarsening, the interfacial area density S_V can be correlated to g_s by an equation of the form

$$S_V = c\, g_s^p (1 - g_s)^q \tag{4}$$

where c, p, and q are constants. According to Eq. (4), with increasing solid fraction S_V first experiences a rise due to the creation of interfacial area by growth, goes through a maximum, and then decreases due to impingement and coalescence of interfaces. Various values for the constants p and q have been suggested. Speich and Fisher [13] found that data from recrystallization experiments could be described by $p = q = 1$. A computational model for the growth and impingement of grains confirmed these exponents [14]. Other suggestions have been $p = q = 2/3$ [15] and $p = q = 1/2$ [16]. A more detailed geometrical model of growing and impinging spheres has revealed that the constants c, p, and q are influenced by the nucleation kinetics and the spatial arrangement of the spheres [17]. Therefore, it is not possible to identify generally valid values for the constants in Eq. (4).

In summary, the basic Eqs. (3) and (4) for the evolution of the interface area are limited to seemingly opposing cases. Eq. (3) is valid only for isothermal conditions ($\dot{T} = 0$, $g_s = \text{const.}$), where the interface area decreases with time due to coarsening. Eq. (4), on the other hand, describes processes where g_s increases due to growth ($\dot{T} \neq 0$), but the interface area does not change when $g_s = \text{const.}$ Hence, the question remains how the two evolution equations can be combined to cover the general case of simultaneous growth and coarsening. Due to the length scales involved with dendrites, both phenomena are important in most alloy solidification processes.

The direct study of the morphological evolution of dendritic microstructures during alloy solidification has become possible due to two relatively recent developments: (i) the availability of computational tools, in particular the phase-field method [18] and high performance parallel computing platforms, to allow three-dimensional simulations to be conducted for realistic material properties and relatively large length and time scales, and (ii) the use of enhanced synchrotron and X-ray facilities to perform tomography in real time during solidification with sufficient resolution to measure the geometry of dendrites. In the present study, phase-field simulations of dendritic solidification of a binary alloy are used to study the variation of the interfacial area with solid fraction and time. The simulations extend our previous results [2] for a single to multiple cooling rates, including an isothermal coarsening case. A new specific interface area evolution equation is proposed that fits the simulation data over the entire range of cooling rates. Then, data from previously performed high-speed synchrotron X-ray tomography solidification [19–22] and isothermal coarsening [23–25] experiments involving different alloy systems are used to validate the general interface evolution equation.

2. Phase-field simulations

2.1. Computational model

The 3D phase-field model used in the present study is the same as in Ref. [2]. For completeness, it is briefly described in the following. We employ the well-established phase-field model for directional solidification of a dilute binary alloy of Echebarria et al. [26], which assumes that the dendrites grow in a constant temperature gradient G that moves at a constant velocity V_p. The model is extended to account for solute diffusion in the solid [27].

The material data used in all simulations of the present study are representative of an Al-Cu alloy. They are given by an initial alloy solute concentration $C_0 = 6$ wt.%, liquidus slope $m = -2.6$ K/wt.%, melting point of pure aluminum $T_m = 660$ °C, partition coefficient $k = 0.14$, solute mass diffusivities in the liquid $D_\ell = 3000\ \mu\text{m}^2/\text{s}$ and solid $D_s = 0.3\ \mu\text{m}^2/\text{s}$, respectively, Gibbs-Thomson coefficient $\Gamma = 0.24\ \mu\text{mK}$, and surface energy anisotropy coefficient $\varepsilon_4 = 0.02$. As illustrated in Fig. 1a, the computational domain covers a 1/8 sector of a dendrite by using available symmetries. The simulation domain has a width of 70 μm, which represents one half of the primary dendrite spacing, and a length in the direction of the temperature gradient of 350 μm. The boundaries are characterized by no-flux conditions. A small paraboloid at the bottom of the domain is used as the initial geometry of the solid. When the dendrite tip impinges on the upper wall, the simulation proceeds and the previously grown structure continues to solidify (see Fig. 3 below). The initial temperature of the liquid is taken as the dendrite tip temperature during steady growth; the dendrite tip undercooling was determined iteratively from preliminary simulations.

The phase-field model was implemented numerically using the parallel FEM library AMDiS [28,29]. It allows for adaptive mesh refinement, an example of which is shown in Fig. 1b. For the base case simulation, the smallest element size was 0.153 μm, which can be compared to a steady state primary dendrite tip radius in the base case simulation of 2.7 μm. The problem size was on average

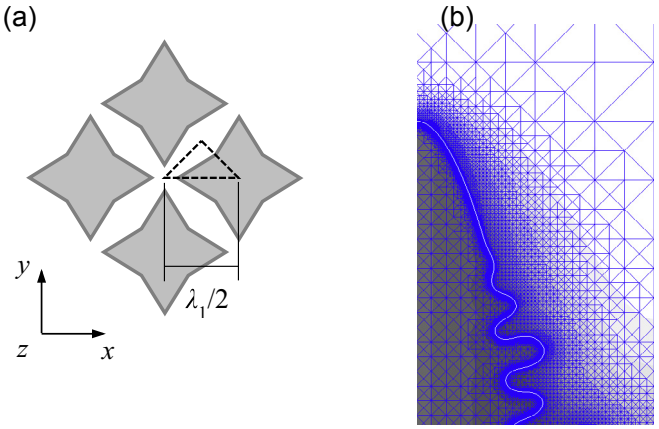

Fig. 1. Computational model: (a) assumed arrangement of the dendrites normal to the temperature gradient and triangular cross section of the calculation domain; (b) example of the adaptive mesh refinement used near the solid-liquid interface.

2.5×10^7 degrees of freedom. A semi-implicit time discretization scheme was employed to allow for adaptation of the time step to the different time scales of the interface dynamics associated with growth and coarsening. The computations were carried out on a high performance computing (HPC) cluster using 512 CPUs. The base case simulation took about one week of time.

Numerous tests were performed to verify that the present results are independent of the diffuse interface thickness and other computational parameters used in the phase-field model. The directional solidification cases in Echebarria et al. [26] were repeated to provide a basic test of the present computations. Additional validation included the simulation of singular events, such as fragmentation of phases due to capillarity. The calculated variation of the neck radius near pinch-off was compared to an exact analytical solution and excellent agreement was obtained [30].

2.2. Base case simulation results

The base case simulation is the same as the one reported in Ref. [2] and corresponds to a pulling speed of $V_p = 300$ μm/s and temperature gradient of $G = 200$ K/cm, resulting in a cooling rate of $\left|\dot{T}_0\right| = 6$ K/s. As will be demonstrated later, at such a high cooling rate the evolution of the interface area is dominated by growth and coalescence, and curvature-driven coarsening is of secondary importance.

Snapshots of the computed dendrite at four different times are shown in Fig. 2 [2]. During the first second (Fig. 2a and b) the primary dendrite tip translates the entire length of the simulation domain. This first stage is characterized by the development of numerous secondary dendrite branches behind the primary tip and a rapid increase in the interface area. At later times (Fig. 2c and d), the volume of solid continues to increase and sidebranches can be observed to coalesce. The impingement of interfaces leads eventually to the development of liquid channels and pockets inside the solid structure (Fig. 2d). The simulation was terminated at $t = 7$ s, which corresponds to a solid volume fraction of $g_s = 0.84$ (see below).

The interface area A and solid volume V_s of the dendrite are evaluated for five different sample volumes along the computational domain, as indicated in Fig. 3a [2]. Their volume $V = 6.52 \times 10^4$ μm^3 is small enough to neglect temperature variations within them, but sufficiently large to avoid excessive scatter in the area and volume measurements. The tilted shape of the sample volumes further aids in suppressing scatter. The measured interface area and solid volume for each sample volume are plotted in Fig. 3 as a function of time [2]. In this figure, $t = 0$ refers to the instant when a portion of the interface enters the sample volume. It can be seen that the center sample volume is most representative of the average variation in A. The center sample volume is used exclusively in the following.

The calculated interfacial area density and inverse specific interface area are plotted against time in Fig. 4a and b, respectively, and against solid fraction in Fig. 4d and e, respectively. The solid fraction variation is shown against time t in Fig. 4c and against dimensionless time θ in Fig. 4f. The dimensionless time (or temperature) is defined as $\theta = (T_\ell - T)/\Delta T_0 = \dot{\theta} t$, in which $T_\ell = T_m + mC_0$ is the liquidus temperature corresponding to the initial solute concentration and $\dot{\theta} = -\dot{T}/\Delta T_0$ is the cooling rate scaled by the equilibrium freezing temperature range $\Delta T_0 = |m| C_0 (1/k - 1)$. Note that the curves in Fig. 4a to c start to increase from zero not until about $t = 0.7$ s, which is the time from the beginning of the simulation when the primary dendrite tip reaches the center sample volume. Based on a detailed analysis, the evolution of the dendrite morphology in Fig. 4 can be divided into three stages.

Stage I is characterized by a steep increase in S_V. This is caused by the initial free dendritic growth and sidebranching creating a large interfacial area, while the melt is still undercooled. Stage I ends at $t = 1$ s when in Fig. 4f the solid fraction curve from the present simulation meets the curves for the classical lever rule and Scheil equation [31]. The latter two predictions assume that the liquid is not undercooled and the primary dendrite tip is located at the equilibrium liquidus temperature. During stage I, the solid fraction increases rapidly from zero to $g_s = 0.3$. Afterwards, the lever rule and Scheil equation closely bound the solid fraction variation from the phase-field simulation [2]. This is expected because the present simulations account for finite-rate solute

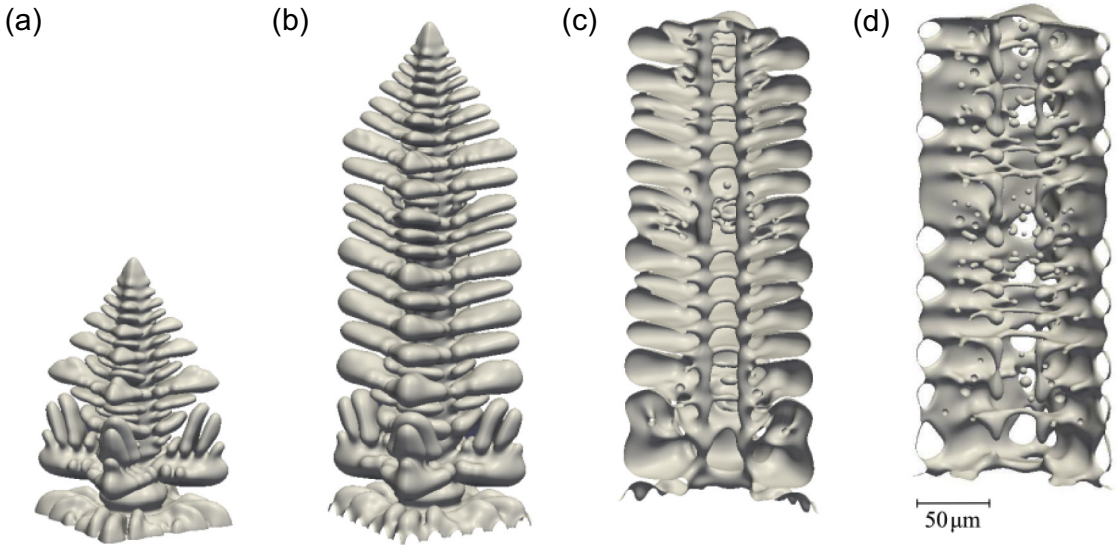

Fig. 2. Evolution of the dendrite geometry for the base case simulation: full view of the growing dendrite at $t = 0.5$ s (a) and 1 s (b); cutaway view of half of the dendrite at $t = 2.5$ s (c) and 7 s (d) [2].

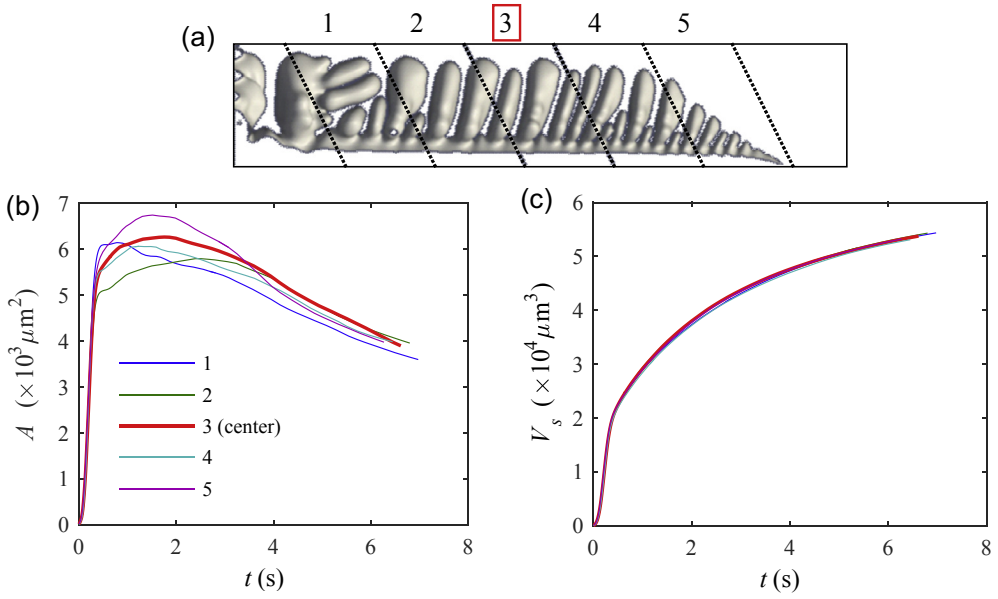

Fig. 3. Sample volumes at different positions along the growth direction (a), and measured evolution of the interface area (b) and solid volume (c) in the sample volumes for the base case simulation [2].

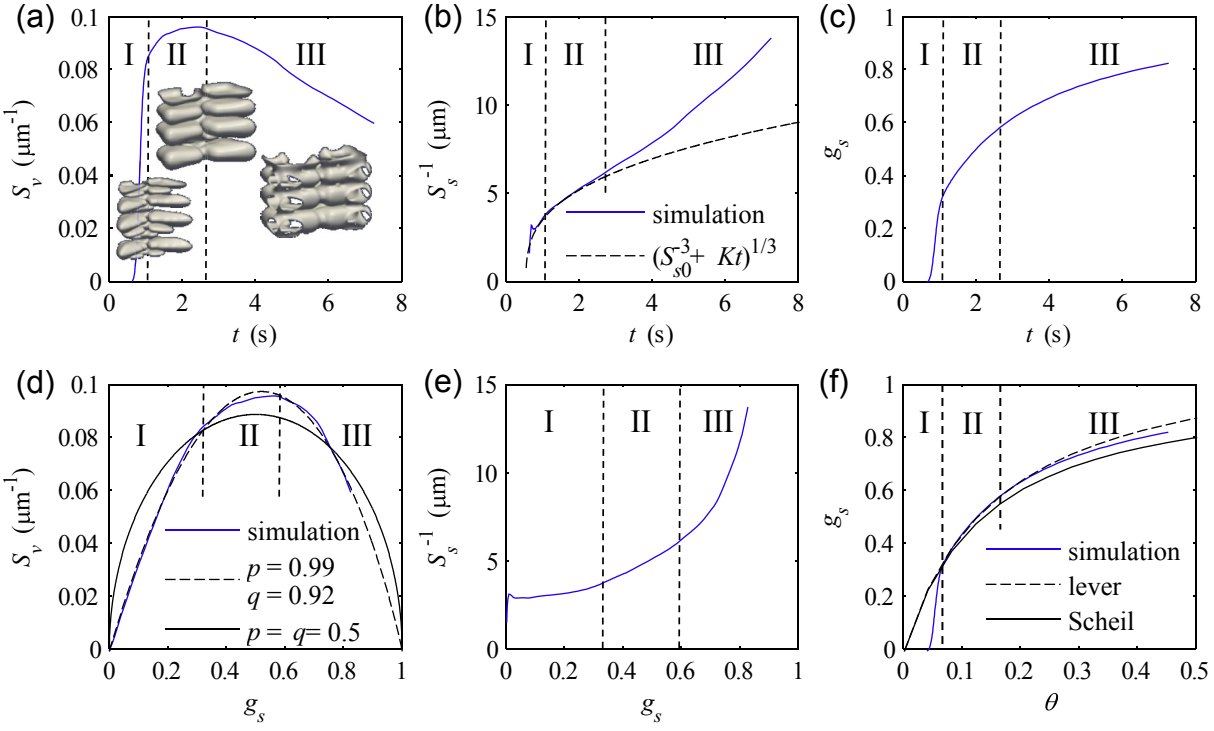

Fig. 4. Base case simulation results: Variation of the interfacial area density with time (a) and solid fraction (d), inverse specific interface area with time (b) and solid fraction (e), and solid volume fraction with time (c) and dimensionless time or temperature (f).

diffusion in the solid, whereas the lever rule and Scheil equation assume infinite and zero diffusion in the solid, respectively.

Although S_s^{-1} increases steeply with time during stage I (Fig. 4b), when plotted against g_s (Fig. 4e) S_s^{-1} is almost constant and equal to about 3–3.6 μm during the entire stage, except at the very beginning. Since the secondary dendrite arms in stage I can be easily identified, it is useful to connect this value of S_s^{-1} with the study of Li and Beckermann [32] who measured geometrical parameters of pure succinonitrile dendrites grown in a microgravity environment. They found that the interfacial area density can be related to the secondary dendrite arm spacing λ_2 by $S_V = 1.6/\lambda_2$. This simple result can be explained by assuming that after some distance from the primary tip, the interfacial area is dominated by the secondary arms and that the sidearms grow in a planar or axial manner. The secondary dendrite arm spacing at the end of stage I ($t = 1$ s) can be estimated from Fig. 2b to be approximately $\lambda_2 = 19$ μm in the

region of the center sample volume (i.e., near mid-height). Hence $S_V = 0.084\ \mu m^{-1}$, which agrees well with the value of $S_V(t = 1\ s)$ in Fig. 4a. Equivalently, the scaling relation of Ref. [32] gives for the inverse specific interface area $S_s^{-1} = g_s/S_V = g_s\lambda_2/1.6 = 3.56\ \mu m$, since $g_s(t = 1\ s) = 0.3$, which is close to the value of $S_s^{-1}(t = 1\ s)$ in Fig. 4b. This agreement with a scaling relation obtained from experimental data lends some confidence to the present phase-field computations. More importantly, being able to predict S_V during stage I from the knowledge of λ_2 allows for the calibration of more general relations for S_V (see the next section). Empirical relations for λ_2 are available for many metal alloys of technological interest (e.g., aluminum alloys, steel) [31].

Stage II is characterized by concurrent growth and coarsening near equilibrium without significant interface coalescence. It ends when S_V in Fig. 4a reaches its maximum value, which occurs at $t = 2.5$ s. Fig. 2c shows the computed dendrite at the end of stage II ($t = 2.5$ s), when the solid fraction is equal to $g_s(t = 2.5\ s) = 0.57$ (Fig. 4c). Another distinct criterion for the end of stage II can be obtained from Fig. 4b. Up until $t = 2.5$ s, the inverse specific interface area varies as $S_s^{-1} \sim t^{1/3}$, as indicated by the dashed line; at later times, it increases at a significantly faster rate. As mentioned in the Introduction, a $t^{1/3}$ law for the evolution of the characteristic interfacial length scale, primarily known for curvature-driven coarsening at constant phase fractions, was also found to be valid for concurrent growth and coarsening in Ref. [12].

During stage III, coalescence of interfaces leads to a decrease in S_V (Fig. 4a) and an increase in S_s^{-1} that is much faster than a $t^{1/3}$ law (Fig. 4b). The interfaces impinge primarily between the thickening secondary dendrite arms (Fig. 2c and d). The coalescence of side-arms also leads to a considerable thickening of the primary stem during stage III.

The plot of the computed interfacial area density S_V against the solid volume fraction g_s in Fig. 4d demonstrates that S_V varies indeed in accordance with Eq. (4). By fitting the present data to Eq. (4), it is found that the exponents are equal to $p = 0.99$ and $q = 0.92$. The proximity of these exponents to $p = q = 1$ found in Ref. [13] for pure growth indicates that curvature-driven coarsening is not important for the relatively high cooling rate used in the base case simulation. Clearly, exponents of $p = q = 0.5$ [19] do not fit the simulation results.

2.3. Effect of cooling rate

New results are now presented where the simulation is extended from a high cooling rate $\dot{T}$ (base case, coarsening of minor importance) toward low $\dot{T}$, including the case $\dot{T} = 0$ such that isothermal coarsening is achieved. The simulations for the lower cooling rates were all restarted from the base case results at the end of stage I ($g_s = 0.3$). This allows one to clearly distinguish between the initial growth of the dendrite in the undercooled melt and the subsequent coarsening and coalescence processes. Restarting the simulation from an intermediate stage is necessary for the isothermal coarsening case, since only an existing solid structure can coarsen. In order to save computational time, the simulations were performed for a reduced computational domain that corresponds approximately to the center sample volume used for the base case (Fig. 2a) but has a rectangular cross section. Cooling rates equal to 1.0, 0.5, 0.1, and 0 times the base case cooling rate were investigated. The results of the simulations are plotted in Fig. 5 using the same structure as in Fig. 4. The lines in the plots of Fig. 5 up to $t = 1$ s or $g_s = 0.3$ are identical for all cooling rates for the reason just explained.

Focusing first on the solid fraction variation with time, Fig. 5c shows that as expected the solid fraction increases more slowly for the lower cooling rates and stays constant at $g_s = 0.3$ for the isothermal case. On the other hand, when plotted against the dimensionless time (Fig. 5f), all solid fraction variations collapse to a single line. This indicates that back diffusion in the solid does not have a significant effect in the present simulations.

As mentioned before, the inverse specific interface area S_s^{-1} is a characteristic length scale of the microstructure. Fig. 5e shows that a reduced cooling rate leads to a coarser microstructure (larger S_s^{-1}) at the same solid fraction. This effect is due to curvature-driven coarsening, which becomes more dominant as the solidification process becomes slower. On the other hand, Fig. 5b indicates that at a given time, the microstructure is finer (smaller S_s^{-1}) for a smaller cooling rate. This can be attributed to the fact that coarsening is a slow process relative to growth and coalescence. In other words, the growth and coalescence that occur for a finite cooling rate increase S_s^{-1} relative to the pure coarsening case when examining the microstructure at the same time.

The interfacial area density S_V versus solid fraction plot in Fig. 5d is perhaps most interesting. The transition between stages II and III, marked by a dot with an arrow, shifts to lower solid fractions when the cooling rate is reduced. This implies that a coarser structure at the same solid fraction is more prone to coalescence. As expected, for the isothermal coarsening case the interfacial area density decreases at a constant solid fraction. For the next lowest normalized cooling rate (0.1), the strong effect of coarsening causes the interfacial area density to never increase after stage I. Clearly, a relation for the interfacial area density of the form of Eq. (4) no longer works when coarsening is important.

3. General interfacial area evolution equation

To be valid for all cooling rates, a general evolution equation for the specific interface area during alloy solidification should combine growth, coarsening and interface coalescence mechanisms. Such a relation must contain both the solid volume fraction and time as independent variables. In solidification processes, the solid fraction can sometimes be related to the temperature through a relation such as the Scheil equation [31], and the temperature may be known as a function of time through the knowledge of the cooling rate. However, this is difficult when the cooling rate is highly variable and impossible during the initial period when the solid grows freely into an undercooled melt, especially if recalescence is involved [31]. Furthermore, during isothermal coarsening, solid fraction and time are completely unrelated. In order to cover all of these diverse mechanisms and cases, the following new relation is proposed here

$$S_s^{-1} = (1 - g_s)^{-r}\left(S_{s0}^{-3} + K_0 t\right)^{1/3} \tag{5}$$

where r, S_{s0}, and K_0 are, at this point, fitting parameters. The second term on the right-hand-side of Eq. (5) has the same form as the classical coarsening law given by Eq. (3). An exponent of $n = 3$ is adopted, since it is valid for concurrent growth and coarsening [12]. The first term accounts for diffusional interactions and interface coalescence, which become increasingly important as the solid volume fraction approaches unity. The strength of both processes is characterized by the exponent r. A least-square fit of the present S_s^{-1} data in Fig. 5 to Eq. (5) yields the following values for the three parameters: $r = 0.4$, $S_{s0}^{-1} = 2.46\ \mu m$ and $K_0 = 23.5\ \mu m^3/s$. Fig. 6a shows that Eq. (5) provides a reasonable fit to the present simulation results for all cooling rates. The values of K_0 and r are discussed in later sections.

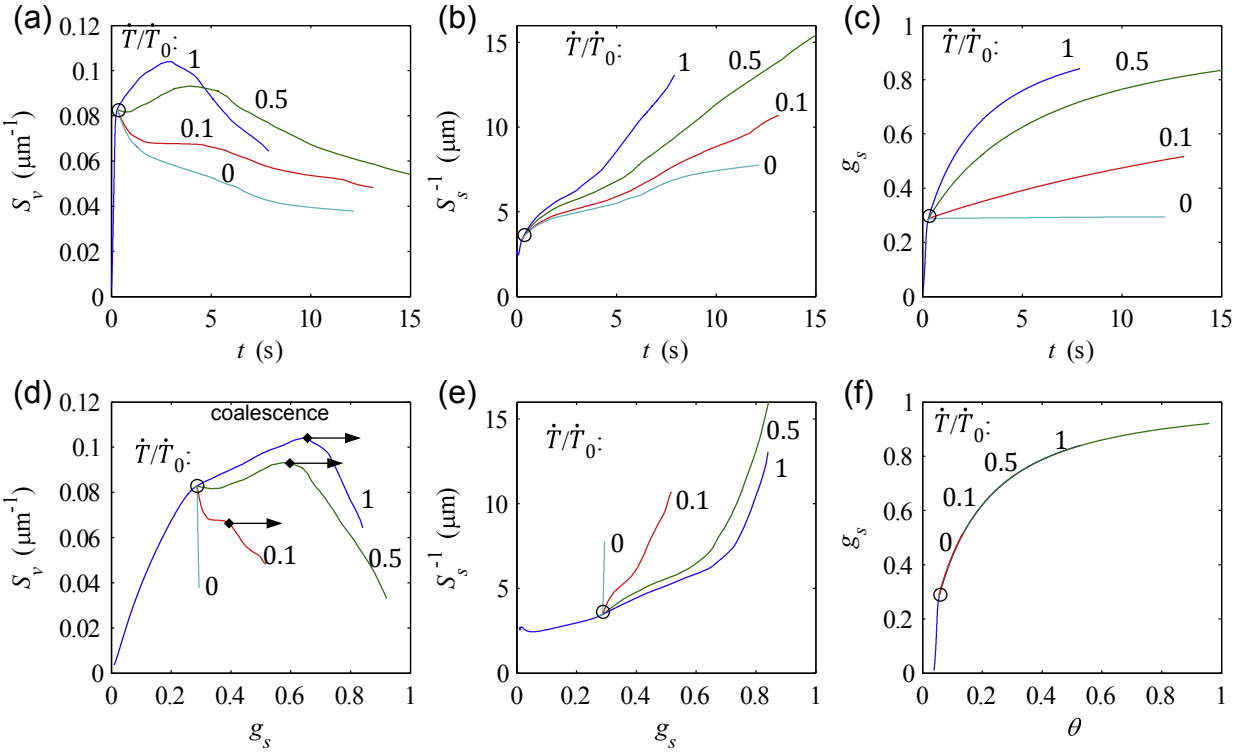

Fig. 5. Computed variations of the interfacial area density, inverse specific interface area, and solid fraction for a step change in the cooling rate at $g_s = 0.3$ (open circle) to three different values. The black dot with an arrow in (d) marks the transition between stages II and III.

According to Eq. (5), S_{s0}^{-1} is the inverse specific interface area or characteristic length scale of the solid at $t = g_s = 0$. This value is generally not defined, since a solid structure of vanishing volume does not have a finite interface area or size. The present finite value for S_{s0}^{-1} (2.46 μm) is simply a result of fitting the data over the entire duration of the simulations. It is interesting to note that this value is close to the present steady-state primary dendrite tip radius of 2.7 μm (see Section 2.1). In the present simulations, $S_s^{-1} = 2.46$ μm is attained after a short time when a few secondary dendrite arms have entered the sample volume (see also Fig. 4b). Note that the initial secondary dendrite arm spacing is closely related to the primary dendrite tip radius [32]. The computed values of S_s^{-1} at earlier times do not affect the fit in a significant way. As demonstrated in the next section, S_{s0}^{-1} can also be used to establish a unique reference time that is equal to $t_0 = S_{s0}^{-3}/K_0$. Shifting time by this reference time then results in $S_s^{-1} = 0$ at $g_s = 0$.

Using Eq. (2), Eq. (5) can be re-written in terms of the interfacial area density as

$$S_V = g_s(1-g_s)^r\left(S_{s0}^{-3} + K_0 t\right)^{-1/3} \tag{6}$$

Note that the first two terms on the right-hand-side of Eq. (6) correspond to Eq. (4) with $p = 1$ and $q = r$. Fig. 6b shows that Eq. (6), with the values of the three parameters from above, fits the predicted S_V from the phase-field simulations reasonably well for all cooling rates, including isothermal coarsening. Some of the discrepancies can be attributed to the use of a reduced computational domain for the simulations in Fig. 6 (for $g_s > 0.3$). This can be

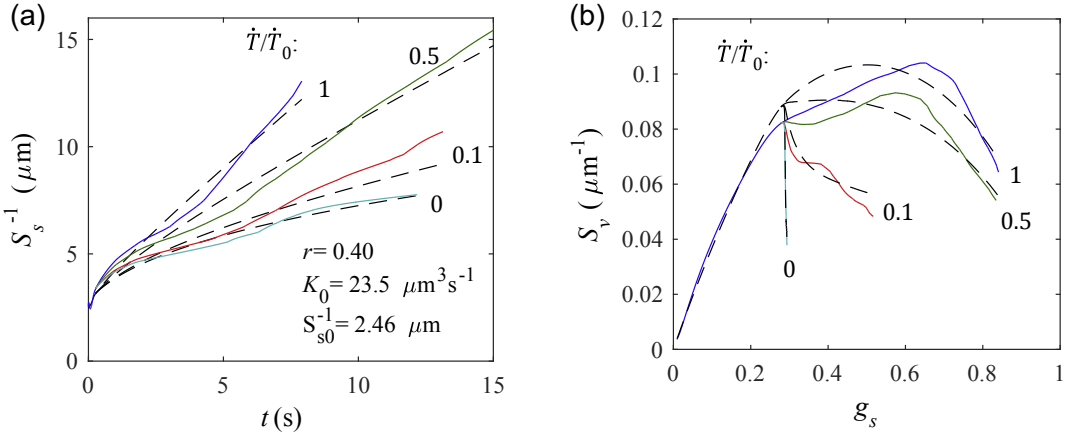

Fig. 6. Fit of the general relation (dashed lines) for the evolution of the inverse specific interface area (a) and the interfacial area density (b) to the phase-field simulation data of Fig. 5 for various cooling rates.

seen by comparing the $S_V(g_s)$ curves for $\dot{T}/\dot{T}_0 = 1$ in Fig. 4d (full domain) and 5d (reduced domain). Hence, the discrepancies in Fig. 6 between the simulation results and the fit should not be overemphasized.

4. Experimental validation using synchrotron X-ray tomography data

The general interfacial area evolution equation, Eq. (5) or Eq. (6), is validated using data from eleven recently performed synchrotron X-ray tomography experiments [19–22]. In these experiments, the interface area and solid volume in a small cell of uniform temperature were measured in real time during solidification. Table 1 lists the main parameters of the experiments. They involve three binary alloy systems (Al-Cu, Mg-Sn, and Mg-Zn) and a wide range of solute concentrations and cooling rates. Experiments D1 to D7 with Mg-Zn alloys are characterized by an initial solidification phase, followed by an approximately isothermal holding phase. Note that the Al alloy dendrites have a cubic crystal lattice, whereas the Mg alloys have a hexagonal lattice.

For each experiment, measurements of the specific interface area were made over a range of solid volume fractions and times. Because meaningful measurements could generally not be performed during the very initial period of solidification, it is not possible to identify the exact time at which the solid fraction starts to increase from zero. This problem was overcome by performing the fit of the data using an arbitrary time scale. The resulting S_{s0}^{-1} is then used to calculate a time shift according to $t_0 = S_{s0}^{-3}/K_0$. A plot of S_s^{-1} versus this shifted time then goes through the origin. The time shift has no effect on the values of the other two fitting parameters, K_0 and r.

Fig. 7 shows the fit of the experimental data to the general interfacial area evolution equation as plots of S_s^{-1} versus shifted time (Fig. 7a and c) and S_V versus solid volume fraction (Fig. 7b and d). Excellent agreement can be observed. The fit is good even for those experiments that feature a highly variable cooling rate and include an isothermal holding phase. This can be attributed to including both the solid volume fraction and time as independent variables in the evolution equation. The values of the fitting parameter K_0 obtained for the eleven experiments are listed in Table 1 and are discussed further in the next section. For all experiments, an exponent of $r = 0.25$ was used. This value gave the best fit for Experiment A, where measurments were made over a solid fraction range from about 0.2 to 0.85. For the other experiments, the value of r has a large uncertainty, because the measurements were made either over a relatively small solid fraction range or only at solid fractions below 0.4 (Experiments B and D1 to D7), where r plays only a minor role. In fact, an exponent of $r = 0.4$, as obtained from the phase-field simulations, would have also resulted in a reasonably good fit for most experiments, except for Experiment A (not shown here for conciseness). The difference in the exponents between the simulations ($r = 0.4$) and the experiments ($r = 0.25$) may be explained by the highly regular and symmetric arrangement of the (columnar) dendrites in the simulations (Fig. 1a). Such an arrangement leads to stronger interface coalescence, a smaller interfacial area density and, hence, a higher exponent r. In contrast, the (equiaxed) dendrites in the experiments were grown freely, in the absence of a temperature gradient, and were oriented randomly. Clearly, the exact dependence of r on the orientation and spacing of the dendrites deserves further investigation.

5. Prediction of the rate constant

Table 1 lists the values of the fitting parameter K_0 obtained for the eleven experiments and the phase-field simulations. While they vary by almost a factor of 50, the K_0 values for each individual alloy composition are close to each other, indicating that K_0 is indeed independent of the cooling rate. A general expression for K_0 in terms of alloy properties may be obtained by realizing from Eq. (5) that K_0 is the constant of proportionality at which the cube of a microstructural length scale, S_s^{-3}, evolves with time at a given solid fraction. According to various theories of growth and coarsening of solid-liquid mixtures [7,8,12], such a rate constant is always proportional to the product of the solute mass diffusivity in the liquid and the capillary length, i.e.,

$$K_0 = aD_\ell d_0 \tag{7}$$

where a is a constant of proportionality. The capillary length for binary alloys at the equilibrium liquidus concentration C_0 is defined as

$$d_0 = \frac{\Gamma}{|m|C_0(1-k)} \tag{8}$$

The present data are used in the following to determine if a unique value for the constant a can be found that links K_0 to alloy properties in accordance with Eq. (7).

The various alloy parameters used to evaluate the product $D_\ell d_0$ are listed in Table 2. For the simulations, they are the same as those provided in Section 2.1 and simply represent popular choices for Al-Cu alloys [33]. For the experiments, the properties m and k were determined at each alloy composition C_0 by taking into account the

Table 1
Summary of the conditions for the phase-field simulations and the synchrotron X-ray tomography solidification experiments, together with the rate constants K_0 resulting from the fit of the data to the general interfacial area evolution equation, Eq. (5). Experiments D1 to D7 are characterized by an initial constant cooling rate up to some solid fraction, followed by isothermal holding. The fits use $r = 0.4$ for the simulations and $r = 0.25$ for the experiments.

	Ref.	Alloy	$\dot{T}$ (K/min)	K_0 ($\mu m^3/s$)
simulations	present work	Al-6wt.%Cu	−360, −180, −36, … 0	23.5
exp. A	[19]	Al-10 wt.%Cu	−3	9.59
exp. B	[20]	Al-24 wt.%Cu	−2	3.05
exp. C1	[21]	Mg-15 wt.%Sn	−3	26.3
exp. C2	[21]	Mg-15 wt.%Sn	−12	24.5
exp. D1	[22]	Mg-25 wt.%Zn	−25 … 0	2.33
exp. D2	[22]	Mg-25 wt.%Zn	−25 … 0	1.91
exp. D3	[22]	Mg-25 wt.%Zn	−3 … 0	2.79
exp. D4	[22]	Mg-38 wt.%Zn	−25 … 0	0.79
exp. D5	[22]	Mg-38 wt.%Zn	−25 … 0	0.62
exp. D6	[22]	Mg-38 wt.%Zn	−3 … 0	0.64
exp. D7	[22]	Mg-38 wt.%Zn	−3 … 0	0.57

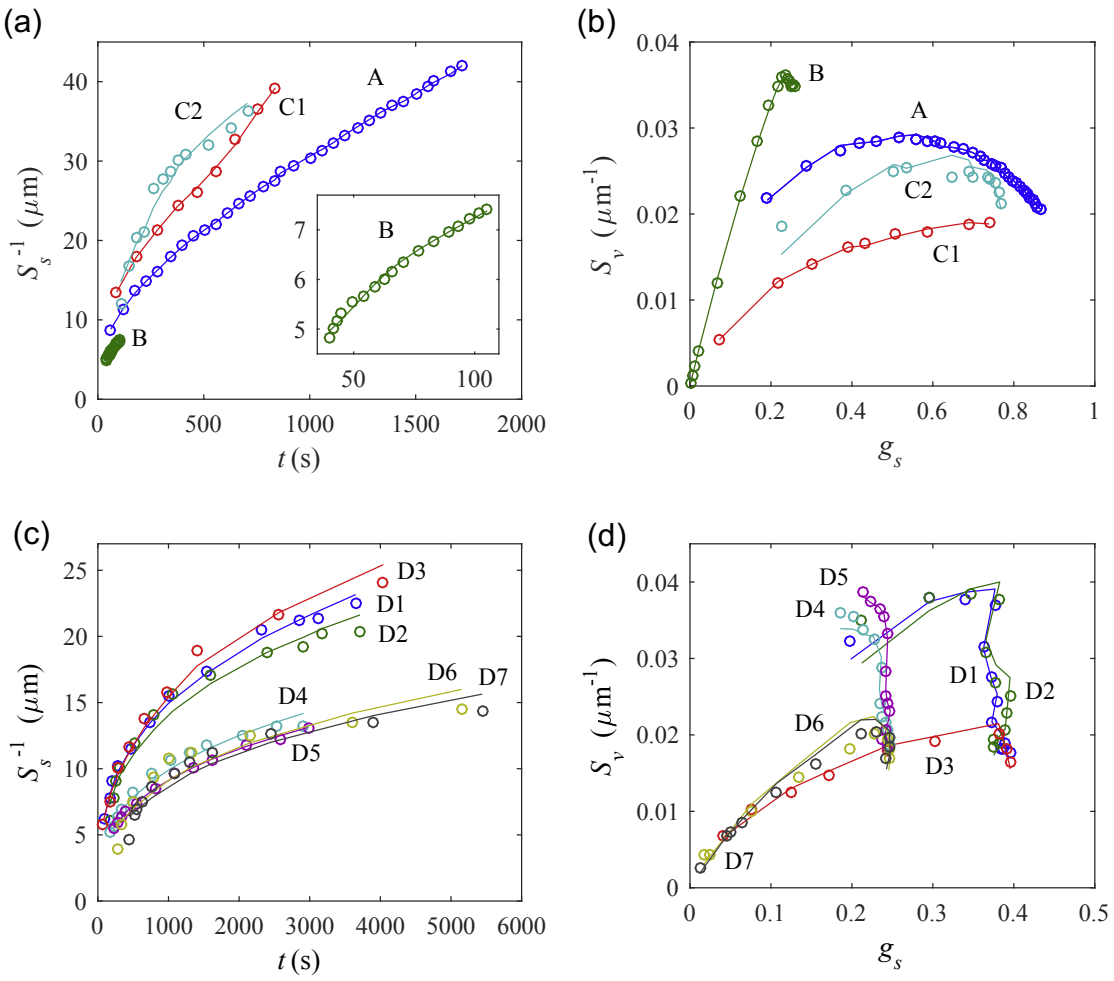

Fig. 7. Fits of the general interfacial area evolution equation (lines) to the synchrotron X-ray tomography experimental data (open circles) referenced in Table 1: (a) and (b) are for experiments A, B, C1 and C2; (c) and (d) are for experiments D1 to D7; (a) and (c) show the inverse specific interface area versus shifted time; (b) and (d) show the interfacial area density versus solid volume fraction. A best matching exponent of $r = 0.25$ was used and the values of K_0 for each experiment are listed in Table 1.

Table 2
Estimated properties for the various alloys.

	C_0 (wt.%)	m (K/wt.%)	k	T (K)	D_ℓ (μm^2/s)	Γ (Kμm)
Simulation (Al-Cu)	6	−2.6	0.14	–	3000	0.24
exp. A (Al-Cu)	10	−3.3	0.13	–	2400	0.24
exp. B (Al-Cu)	24	−4.3	0.16	–	2400	0.24
exp. C1-2 (Mg-Sn)	15	−2.0	0.3	853	6171	0.141
exp. D1-3 (Mg-Zn)	25	−6.7	0.12	763	4146	0.147
exp. D4-7 (Mg-Zn)	38	−9.3	0.13	683	2665	0.151

varying slopes of the liquidus and solidus lines in the relevant equilibrium phase diagrams [34]. For the Al-Cu experiments, the value for D_ℓ reflects the results of recent experiments [35]. For the Mg-Zn experiments, D_ℓ was estimated using data from Wang et al. [36]: theoretical predictions of the inter-diffusion coefficient in liquid Mg-Zn alloys at the melting point of pure Mg, which are relatively independent of solute content, were extrapolated to the approximate average temperature T in the experiments (also listed in Table 2) using the Arrhenius exponent for self-diffusion of pure Mg. Since inter-diffusion coefficients for Mg-Sn could not be identified in the literature, the same data and procedure as for Mg-Zn was utilized. The Gibbs-Thomson coefficient Γ for the Al-Cu alloys was taken from Ref. [33]. For the Mg alloys, Γ was estimated as the value for pure Mg using the data and equations listed in Table 3. According to the data in Ref. [38], the surface tension for Mg-Zn alloys on the Mg-rich side is only weakly dependent on the solute content, justifying the use of pure Mg data. The slight temperature dependence of the Γ values for Mg in Table 2 stems from the temperature dependent properties in Table 3.

Fig. 8 shows a plot of the present K_0 values from Table 1 against the product $D_\ell d_0$. It can be seen that Eq. (7) predicts the rate constant well, with $a = 0.53 \pm 0.084$ obtained from a least-square fit. The deviations from Eq. (7) can easily be explained by uncertainties in the experiments and the alloy properties. Since the uncertainties in the properties are largest for the Mg alloys, another fit was performed using the Al alloy data only. This fit (not shown here for conciseness) gave $a = 0.46 \pm 0.021$, which is well within the uncertainty of the value from the fit of all datasets.

Table 3
Thermodynamic and surface properties of pure Mg.

Parameter	Symbol	Value/Relation	Units	Ref.
Melting temperature	T_m	922	K	[34]
Molar mass	M	24.305	g/mol	[34]
Latent heat at T_m	L_m	8790	J/mol	[34]
Liquid density	ρ	$1590 - 0.26\,(T - T_m)$	kg/m^3	[34]
Interface energy liquid/vapor	γ_{LV}	$0.556 - 35 \times 10^{-5}(T - T_m)$	J/m^2	[34]
Interface energy solid/liquid	γ_{SL}	$0.1525\ \gamma_{LV}$	J/m^2	[37]
Gibbs-Thomson coefficient	Γ	$\gamma_{SL} T_m/(L_m \rho/M)$	K m	[31]

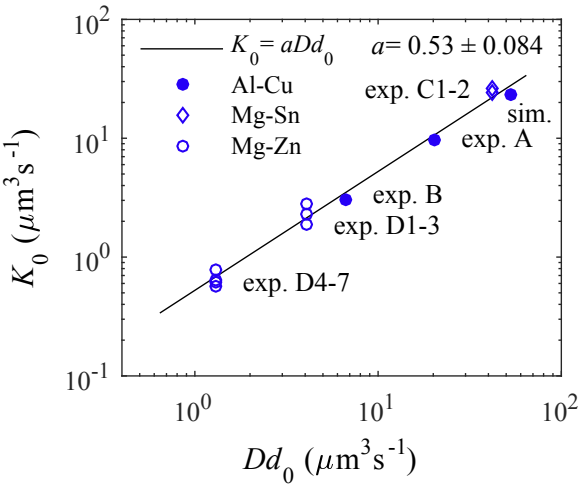

Fig. 8. Variation of the rate constant K_0 with alloy properties $D_\ell d_0$, using $r = 0.4$ for the simulations and $r = 0.25$ for the experiments.

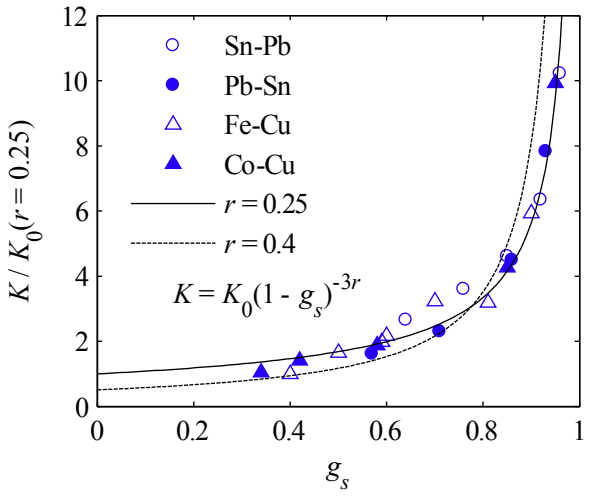

Fig. 9. Comparison of measured and predicted variation of the normalized coarsening rate constant K with solid volume fraction. The predictions are from Eq. (9) for $r = 0.25$ (solid line) and $r = 0.4$ (dashed line). The data points are from isothermal coarsening experiments on dispersed solid-liquid mixtures of Sn-Pb [23], Pb-Sn [23], Fe-Cu [24,25], and Co-Cu [25] alloys.

6. Isothermal coarsening limit

The general interfacial area evolution equation should also be valid for the limiting case of isothermal coarsening at a constant solid volume fraction. Comparing Eq. (5) to the classical coarsening law given by Eq. (3) yields for the coarsening rate constant

$$K = K_0(1 - g_s)^{-3r} \tag{9}$$

Hence, K_0 can be interpreted as a coarsening rate constant in the limit of vanishing solid fraction. Eq. (9) then provides a relation for the dependence of the coarsening rate constant on the solid fraction.

Fig. 9 shows a comparison of Eq. (9) with experimental data for the coarsening rate constant as a function of the solid volume fraction as collected by Voorhees [9]. The data are from isothermal coarsening experiments on dispersed solid-liquid mixtures of Sn-Pb [23], Pb-Sn [23], Fe-Cu [24,25], and Co-Cu [25] alloys. Excellent agreement between the measurements and the present prediction can be observed for $r = 0.25$. It can be seen that even with $r = 0.4$, Eq. (9) fits the experimental coarsening date reasonably well. The exact morphology and arrangement of the solid particles in the isothermal coarsening experiments is not known, but it can be expected to be rather random and not aligned. Therefore, it is not surprising that the exponent $r = 0.25$ from the synchrotron X-ray tomography experiments, involving randomly arranged equiaxed dendrites, fits the isothermal coarsening data better. Recall that the exponent from the present phase-field simulations, $r = 0.4$, was obtained for highly aligned and symmetric columnar dendrites. In summary, the present general interfacial area evolution equation is not only valid in the limit of isothermal coarsening, but it also provides the correct solid fraction dependency of the coarsening rate constant. It is interesting to note that, even though the exponent r was obtained, in part, from experiments or simulations where curvature-driven coarsening is of minor importance, it is the same as in pure (isothermal) coarsening.

7. Conclusions

Phase-field simulations have been performed of columnar solidification of a binary alloy in order to study the evolution of the interface area of an assembly of dendrites. Three stages in the evolution of the interface area can be distinguished. During stage I, the dendrites grow in a melt that is still undercooled and the interface area and the solid volume fraction increase sharply with time. Towards the end of stage I, the interfacial area density may be related to the secondary dendrite arm spacing through $S_V = 1.6/\lambda_2$. During stage II, the inverse specific interface area evolves with time as $S_s^{-1} \sim t^{1/3}$, regardless of cooling rate. At the end of stage II, the interfacial area density reaches a maximum. During stage III, the interfacial area density decreases due to coalescence of interfaces.

A general evolution equation for the specific interface area, Eq. (5), or the interfacial area density, Eq. (6), during dendritic alloy solidification has been developed and validated using data from both the present phase-field simulations and synchrotron X-ray tomography and isothermal coarsening experiments available in the literature. This equation contains both the solid volume fraction and time as independent variables. It is shown to be valid for arbitrary and variable cooling rates, including isothermal

coarsening, and a wide range of (binary) alloys.

The present evolution equation contains three fitting parameters: S_{s0}^{-1}, K_0, and r. The initial inverse specific interface area S_{s0}^{-1} represents an initial length scale of the microstructure. Although this parameter is generally not defined at the beginning of solidification, the simulations show that it can be taken equal to the primary dendrite tip radius. Alternatively, S_{s0}^{-1} can be used to establish a unique reference time at which $S_s^{-1} = 0$. The rate constant is given in terms of alloy properties by $K_0 \approx 0.5 D_\ell d_0$, as verified by both simulation and experimental data covering a wide range of cooling rates and alloy systems. The experimental data for both solidification and isothermal coarsening suggest an exponent r equal to 0.25. However, for the highly regular and symmetric dendrite arrangement assumed in the phase-field simulations, $r = 0.4$ provides a better fit.

Future research should be aimed at investigating in more detail the dependence of the interaction and coalescence exponent r on the arrangement and spacing of the dendrites. For example, for columnar solidification the exponent can be expected to depend on the spacing of the primary dendrite trunks, which in turn is a function of the cooling rate and the temperature gradient [31]. For equiaxed solidification, the number density of grains depends on the cooling rate. For a high grain density the growth can be globular rather than dendritic [31], which can be expected to result in a high r. The present evolution equation should also be examined for higher solid fractions, exceeding 0.85. Often, additional phases (e.g., eutectic) form at such high solid fractions, and it is unclear how the present interfacial area evolution equation would perform in those cases. Extension of the equation to multi-component alloys and to account for melt convection would also be of great interest.

Acknowledgements

This work was financially supported by the Helmholtz Association in form of the Helmholtz-Alliance “LIMTECH” and NASA (NNX14AD69G). We thank the supercomputing center in Jülich (HDR08) for providing computing time.

References

[1] M. Asta, C. Beckermann, A. Karma, W. Kurz, R. Napolitano, M. Plapp, G. Purdy, M. Rappaz, R. Trivedi, Solidification microstructures and solid-state parallels: recent developments, future directions, Acta Mater. 57 (2009) 941–971.
[2] H. Neumann-Heyme, K. Eckert, C. Beckermann, Evolution of specific interface area in dendritic alloy solidification, IOP Conf. Ser. Mater. Sci. Eng. 84 (2015) 012072.
[3] S.P. Marsh, M.E. Glicksman, Overview of geometric effects on coarsening of mushy zones, Metall. Mater. Trans. A 27 (1996) 557–567.
[4] R. Mendoza, J. Alkemper, P. Voorhees, The morphological evolution of dendritic microstructures during coarsening, Metall. Mater. Trans. A 34 (2003) 481–489.
[5] J. Ni, C. Beckermann, A volume-averaged two-phase model for solidification transport phenomena, Metall. Trans. B 22 (1991) 349–361.
[6] A.E. Scheidegger, The Physics of Flow through Porous Media, second ed., University of Toronto Press, Toronto, Canada, 1974.
[7] I.M. Lifshitz, V.V. Slyozov, The kinetics of precipitation from supersaturated solid solutions, J. Phys. Chem. Solids 19 (1961) 35–50.
[8] C. Wagner, Theorie der Alterung von Niederschlaegen durch Umlösen (Ostwald Reifung), Z. Elektrochem 65 (1961) 581–591.
[9] P.W. Voorhees, Ostwald ripening of two-phase mixtures, Annu. Rev. Mater. Sci. 22 (1992) 197–215.
[10] W.W. Mullins, The statistical self-similarity hypothesis in grain growth and coarsening, J. Appl. Phys. 59 (1986) 1341–1349.
[11] S.P. Marsh, M.E. Glicksman, Kinetics of phase coarsening in dense systems, Acta Mater. 44 (1996) 3761–3771.
[12] L. Ratke, C. Beckermann, Concurrent growth and coarsening of spheres, Acta Mater. 49 (2001) 4041–4054.
[13] G. Speich, R. Fisher, Recrystallization, Grain Growth and Textures, ASM, Materials Park, OH, 1966.
[14] C.W. Price, Simulations of grain impingement and recrystallization kinetics, Acta Metall. 35 (1987) 1377–1390.
[15] J.W. Cahn, The significance of average mean curvature and its determination by quantitative metallography, Trans. Metall. Soc. AIME 239 (1967) 610–616.
[16] L. Ratke, A. Genau, Evolution of specific surface area with solid fraction during solidification, Acta Mater. 58 (2010) 4207–4211.
[17] A. Almansour, K. Matsugi, T. Hatayama, O. Yanagisawa, Modeling of growth and impingement of spherical grains, Mater. Trans. JIM 37 (1996) 1595–1601.
[18] W.J. Boettinger, J.A. Warren, C. Beckermann, A. Karma, Phase-field simulation of solidification, Annu. Rev. Mater. Res. 32 (2002) 163–194.
[19] N. Limodin, L. Salvo, E. Boller, M. Suery, M. Felberbaum, S. Gailliegue, K. Madi, In situ and real-time 3-D microtomography investigation of dendritic solidification in an Al–10wt.% Cu alloy, Acta Mater. 57 (2009) 2300–2310.
[20] J.W. Gibbs, K.A. Mohan, E.B. Gulsoy, A.J. Shahani, X. Xiao, C.A. Bouman, M. De Graef, P.W. Voorhees, The three-dimensional morphology of growing dendrites, Sci. Rep. 5 (2015) 11824.
[21] S. Shuai, E. Guo, A.B. Phillion, M.D. Callaghan, T. Jing, P.D. Lee, Fast synchrotron X-ray tomographic quantification of dendrite evolution during the solidification of Mg-Sn alloys, Acta Mater. 118 (2016) 260–269.
[22] E. Guo, A.B. Phillion, B. Cai, S. Shuai, D. Kazantsev, T. Jing, P.D. Lee, Dendritic evolution during coarsening of Mg-Zn alloys via 4D synchrotron tomography, Acta Mater. 123 (2017) 373–382.
[23] S.C. Hardy, P.W. Voorhees, Ostwald ripening in a system with a high volume fraction of coarsening phase, Metall. Trans. A 19 (1988) 2713–2721.
[24] A.N. Niemi, T.H. Courtney, Microstructural development and evolution in liquid-phase sintered Fe-Cu alloys, J. Mater. Sci. 16 (1981) 226–236.
[25] S.S. Kang, D.N. Yoon, Kinetics of grain coarsening during sintering of Co-Cu and Fe-Cu Alloys with low liquid contents, Metall. Trans. A 13 (1982) 1405–1411.
[26] B. Echebarria, R. Folch, A. Karma, M. Plapp, Quantitative phase-field model of alloy solidification, Phys. Rev. E 70 (2004) 061604.
[27] M. Ohno, K. Matsuura, Quantitative phase-field modeling for dilute alloy solidification involving diffusion in the solid, Phys. Rev. E 79 (2009) 031603.
[28] A. Voigt, T. Witkowski, A multi-mesh finite element method for Lagrange elements of arbitrary degree, J. Comput. Sci. 3 (2012) 420–428.
[29] T. Witkowski, S. Ling, S. Praetorius, A. Voigt, Software concepts and numerical algorithms for a scalable adaptive parallel finite element method, Adv. Comput. Math. 41 (2015) 1145–1177.
[30] H. Neumann-Heyme, K. Eckert, C. Beckermann, Dendrite fragmentation in alloy solidification due to sidearm pinch-off, Phys. Rev. E 92 (2015), 060401(R).
[31] J.A. Dantzig, M. Rappaz, Solidification, second ed., EPFL Press, Lausanne, Switzerland, 2009.
[32] Q. Li, C. Beckermann, Scaling behavior of three-dimensional dendrites, Phys. Rev. E 57 (1998) 3176–3188.
[33] W. Kurz, D.J. Fisher, Fundamentals of Solidification, fourth ed., CRC Press, Uetikon-Zuerich, Switzerland; Enfield, N.H, 1998.
[34] W.F. Gale, T.C. Totemeier, Smithells Metals Reference Book, eighth ed., Butterworth-Heinemann, Amsterdam, 2004.
[35] J. Lee, S. Liu, H. Miyahara, R. Trivedi, Diffusion-coefficient measurements in liquid metallic alloys, Metall. Mater. Trans. B 35 (2004) 909–917.
[36] S. Wang, D. Liu, Y. Du, L. Zhang, Q. Chen, A. Engström, Development of an atomic mobility database for liquid phase in multicomponent Al alloys: focusing on binary systems, Int. J. Mater. Res. 104 (2013) 721–735.
[37] W. Tyson, W. Miller, Surface free energies of solid metals: estimation from liquid surface tension measurements, Surf. Sci. 62 (1977) 267–276.
[38] N. Jha, A.K. Mishra, Thermodynamic and surface properties of liquid Mg–Zn alloys, J. Alloys Compd. 329 (2001) 224–229.